Journal of
Biomedical Optics

SPIEDigitalLibrary.org/jbo

# Multiphoton fluorescence, second harmonic generation, and fluorescence lifetime imaging of whole cleared mouse organs

Sam Vesuna
Richard Torres
Michael J. Levene

SPIE

Journal of Biomedical Optics 16(10), 106009 (October 2011)

# Multiphoton fluorescence, second harmonic generation, and fluorescence lifetime imaging of whole cleared mouse organs

**Sam Vesuna,[a] Richard Torres,[a,b] and Michael J. Levene[a]**
[a]Yale University, Department of Biomedical Engineering, 55 Prospect St., New Haven, Connecticut 06511
[b]Yale School of Medicine, Department of Laboratory Medicine, 330 Cedar St., New Haven, Connecticut 06511

**Abstract.** Multiphoton microscopy of cleared tissue has previously been demonstrated to generate large three-dimensional (3D) volumetric image data on entire intact mouse organs using intrinsic tissue fluorescence. This technique holds great promise for performing 3D virtual biopsies, providing unique information on tissue morphology, and guidance for subsequent traditional slicing and staining. Here, we demonstrate the use of fluorescence lifetime imaging in cleared organs for achieving molecular contrast that can reveal morphologically distinct structures, even in the absence of knowledge of the underlying molecular source. In addition, we demonstrate the power of multimodal imaging, combining multiphoton fluorescence, second harmonic generation, and lifetime imaging to reveal exceptional morphological detail in an optically cleared mouse knee. *© 2011 Society of Photo-Optical Instrumentation Engineers (SPIE).* [DOI: 10.1117/1.3641992]

Keywords: fluorescence microscopy; multiphoton microscopy, medical optics; nonlinear microscopy; tissue characterization.

Paper 11277R received Jun. 1, 2011; revised manuscript received Aug. 23, 2011; accepted for publication Aug. 31, 2011; published online Oct. 3, 2011.

## 1 Introduction

The prospect of three-dimensional (3D) reconstruction of tissue specimens with sub-cellular resolution has been of considerable interest to researchers and practicing pathologists. A multitude of approaches for three-dimensional reconstruction of tissue sections have been employed including optical coherence tomography,[1,2] confocal microscopy,[3] multiphoton microscopy (MPM),[4,5] histology sectioning with image scanning,[6] and radiological methods such as microcomputed tomography[7,8] and even MRI.[9] Each has advantages but significant limitations. Radiologic methods can be used *in vivo*, but cellular resolution of tissue is not readily achievable. Histology sectioning produces easily recognizable morphology, but is labor intensive and destructive, as well as somewhat limited in $z$-resolution. For other nonradiologic methods, a significant challenge has been overcoming depth limitations. Typical best results are imaging at depths of $\sim 100\ \mu$m, which can be attained with MPM in fixed tissue. Some investigators have combined MPM with serial sectioning[10] or tissue ablation[11] as an approach to three-dimensional reconstruction, but the process is laborious and cumbersome and results in the destruction of the tissue sample, precluding both subsequent use in conventional pathological processing and storage for repeated inspection.

While the optical sectioning capability, superior contrast, and minimal photodamage of MPM make it the ideal choice for deep tissue imaging of intrinsic fluorescence in biological tissues,[12–14] its limited imaging depth remains a barrier. Regenerative amplifiers[15] and the use of longer wavelength excitation,[16] near 1300 nm, have both been employed with MPM to increase imaging depth. However, high-repetition-rate regenerative amplifiers add considerable cost and complexity, and are not wavelength tunable, thus severely limiting their application. Longer-wavelength excitation is also limited by a scarcity of appropriate dyes and is not appropriate for intrinsic fluorescence excitation. Neither approach has been attempted using fixed tissue, which has a significantly shorter photon scattering length compared to live tissue. The limitations of MPM depth penetration can be ameliorated by reducing light scattering created by the refractive index mismatch of tissue and water. This can be achieved by index matching the fluid portion of a specimen by replacing water with a 1:2 mixture of benzyl alcohol:benzyl benzoate.[17] The tissue clarification method has been used successfully with several different imaging modalities.[18–20] In particular, MPM of clarified tissue offers the advantages of adjustable fields of view (dependent on objective), high resolution, high tolerance to residual scattering (improving imaging depth), and the potential for simultaneous use of other noninvasive imaging modalities, such as second harmonic generation (SHG), that also do not require any additional stains or specimen manipulation.[4]

Recently, MPM of intrinsic fluorescence and SHG from optically cleared tissue has been shown to achieve subcellular resolution several millimeters below the surface of fixed tissues.[4] While intrinsic fluorescence and SHG are the most promising sources of contrast for potential clinical application to the development of three-dimensional histology of human biopsy tissue, most intrinsic fluorophores display broad, overlapping emission and absorption spectra that greatly complicate efforts to distinguish different molecular sources of fluorescence. In addition, the molecular sources of intrinsic fluorescence present in a sample are often unknown. Steady-state multiwavelength

---

Address all correspondence to: Michael Levene, Yale University, Biomedical Engineering, 55 Prospect St., 312 Malone Engineering, Center, New Haven, Connecticut 06511; Tel: 203-432-4264; E-mail: Michael.Levene@Yale.edu.

1083-3668/2011/16(10)/106009/6/$25.00 © 2011 SPIE

methods have been used to differentiate intrinsic fluorophores by unmixing their fluorescence spectra.[19–23] However, these methods work best when the underlying molecular sources of contrast and their spectra are known. In practice, it is often very difficult to determine the molecular source of intrinsic tissue fluorescence. Nonetheless, the spatial distribution of unidentified fluorescent sources may correlate with important morphological details, making their resolution important even if their identity remains unknown.

Fluorescence lifetime imaging (FLIM) is a highly sensitive, time-resolved technique that uses the lifetime of the fluorophore signal, rather than its intensity, to generate an image. The lifetime of a fluorophore is dependent on both the radiative and nonradiative rates of decay from the excited state. While the radiative rate is only weakly dependent on the environment, the nonradiative rate depends upon energy transfer between the excited molecule and its environment, making it a sensitive indicator of environmental changes. FLIM can be used to map fluorophore localization, cellular metabolic states, *p*H, and oxygen saturation.[24] For example, previous studies have revealed that reduced nicotinamide adenine dinucleotide (phosphate), NAD(P)H, exhibits multiple lifetimes in the brain[25,26] and show clear segregation of NAD(P)H within a cell depending on its binding state.[27] FLIM can therefore not only distinguish molecules that have largely-overlapping spectra and different lifetimes, but can additionally distinguish differences in the environment surrounding the same fluorophore.

Here we present MPM, SHG, and FLIM images and 3D data sets from intact, fixed, cleared mouse testicle and knee. Images from a mouse testicle demonstrate the ability of FLIM to distinguish known molecular sources, in this case elastin and NAD(P)H, that have broadly overlapping emission spectra.[28,29] Images from a mouse knee demonstrate the ability of a multimodal combination of MPM, SHG, and FLIM to reveal exquisite morphological details of complex structures and the use of FLIM to distinguish useful morphology even when the source of fluorescence is not known. Large volumetric data stacks from both the testicle and knee are presented, demonstrating the ability to resolve complex three-dimensional structures.

## 2 Materials and Methods

### 2.1 *Organ Preparations*

C57 black mice (1 to 3 months old) were anesthetized with an intraperitoneal injection of ketamine/xylazine (100 mg/kg: 10 mg/kg). The mice were restrained to a surgical bed. Following an incision made below the xyphoid process, the mice were perfused through the heart with phosphate buffer saline (PBS) at 4°C. A perfusion of 4% paraformaldehyde (PFA) followed immediately until the body became tangibly stiffer.

The tissue was cleared using a previously described method.[4] Briefly, the intact leg and testicle were left in PFA for at least 12 h to allow for complete fixation. The samples were rinsed twice with PBS at room temperature and subsequently dehydrated via a graded methanol assay (50%, 70%, 95%, 100%, 100%). A graded ethanol series may also be used, however, this takes about 5 times longer. After each step (30 min), each vial was drained of solution and immediately refilled with the next methanol solution in the series.

Organs were cleared using a solution of 1:2 benzyl alcohol to benzyl benzoate (BABB). After the methanol dehydration, tissue was placed in a 1:1 solution of methanol:BABB for 4 h. The 1:1 solution was then replaced with 100% BABB solution. Imaging was performed after 24 h in BABB at room temperature, at which time tissue was noticeably cleared. The tissue may also be cleared using a solution of methylsalicylate, however, we observed better results in most tissue with BABB.

### 2.2 *Imaging*

Images were captured using a previously described custom-built multiphoton microscope based on the Olympus BX51 WI upright fluorescence microscope (Olympus America, Center Valley, Pennsylvania) equipped with a 5× Nikon objective lens with 0.5 numerical aperture (AZ Plan Fluor, Nikon Corp., Tokyo, Japan).[4] The excitation source was an 80 MHz pulsed Ti:Sapphire laser (Mai Tai, Spectra-Physics, Mountain View, California) tunable between 710 and 990 nm. The excitation wavelength was 740 nm with a ∼100 fs pulse width. Samples were placed on a 3-axis microscope stage (ASI Imaging, Eugene, Oregon).

FLIM was achieved via the addition of a multichannel plate PMT (R3809U-52, Hamamatsu) with a 150 ps rise time and a time-correlated single photon counting card (SPC-150, Becker and Hickl, Berlin, Germany). The Becker and Hickl software, SPC Image, calculated fluorescent lifetimes on a pixel-by-pixel basis by fitting every pixel to a one-, two-, or three-component fluorescence decay fit. The number of components in each fit was determined by choosing the fit with the lowest $\chi^2$ value. Images were captured at a rate of 2.5 frames/s.

Autofluorescence was filtered through a 460/80 bandpass filter, and second harmonic generation was filtered through a 370/20 bandpass filter (Chroma Technologies, Rockingham, Vermont). Photomultiplier tubes (HC-125-02, Hamamatsu, Bridgewater, New Jersey) were used to collect both spectra. *z*-stacks were collected in 5 $\mu$m steps and processed using SCANIMAGE software.[30] The depth was quantified by zeroing the stage at the tissue's surface before capturing images within the tissue volume. Movies of rotating image stacks were created using IMAGEJ software with autoscaling, resulting in the appearance of some flicker during stack rotation.

### 2.3 *Histology*

Traditional histology slide preparation was performed by standard methods: paraformaldehyde-fixed, BABB-clarified specimens were placed in histology cassettes after MPM/SHG/FLIM imaging, processed for paraffin wax embedding using an unmodified automated progressive "dehydration" protocol (Shandon Excelsior Tissue Processor), followed by cutting into 5-$\mu$m thick sections for mounting on slides. Hematoxylin and eosin (H&E) staining was performed using standard manual technique.

## 3 Results

Intrinsic fluorescence images of paraformaldehyde-fixed, BABB-cleared testes obtained by multiphoton microscopy showed cellular detail more than 1-mm deep into tissue. Optical clearing appeared to slightly increase tissue autofluorescence

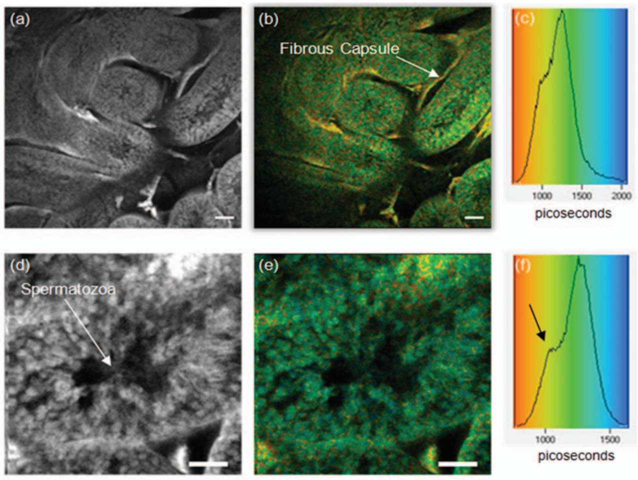

**Fig. 1** Single frame excerpts from image stack of (a) and (d) fluorescence intensity (Video 1) and (b) and (e) color coded images (Video 2) of seminiferous tubules in mouse testicle at depth of 800 $\mu$m with (c) and (f) corresponding lifetime histograms. Scale bars = 100 $\mu$m (a) and (b), 25 $\mu$m (d) and (e). Arrow in (f) points to the presence of a distinct short lifetime present corresponding to elastin in surrounding capsules. (Video 1, MPEG, 4.27 MB) [URL: http://dx.doi.org/10.1117/1.3641992.1]; (Video 2, MPEG, 1.08 MB) [URL: http://dx.doi.org/10.1117/1.3641992.2]

but did not significantly affect the emission spectra. The graded methanol dehydration series did not change morphology or connective tissue structure, but did reduce tissue size by approximately 20%. Spermatocytes maturing to spermatozoa are readily identified within seminiferous tubules at 800 $\mu$m [Figs. 1(a) and 1(d)]. Fluorescence lifetime imaging produced clear images at the same depth showing an expected high contrast between seminiferous tubules and the surrounding elastic smooth muscle capsule [Figs. 1(b) and 1(e)]. In the Becker&Hickl lifetime histograms [Figs. 1(c) and 1(f)], two distinct lifetimes of approximately 1.0 and 1.3 ns are present, corresponding to elastin in smooth muscle and intracellular NAD(P)H, respectively.

High resolution multiphoton images of a maturing mouse knee also showed cellular detail in fixed, BABB-cleared whole leg specimens at depths greater than 1 mm. In virtual sections, the low intrinsic fluorescence of bone allows a clear definition of individual chondrocytes (cartilage cells) forming the articular cartilage surface [Fig. 2(a) and inset].

Osteocytes (bone cells) are visible as regularly spaced punctate bright spots in the portions of outer bone (periosteum) present [Fig. 2(a)]. The fibrous organization of the meniscus overlying the chondrocytes is identifiable. Autofluorescent bone marrow hematopoietic cells form irregular aggregates demarcated by dark bony spicules in the subchondral portion of the developing bone (secondary ossification center). The corresponding H&E stained slide from the same sample is shown [Fig. 2(b)], illustrating the comparable resolution and complementary information the multiphoton image provides. Note that the thinned meniscus at this depth is displaced during the cutting process of the stained slide but remains visible *in situ* in the cleared MPM image.

Serial virtual sections using multiphoton intrinsic fluorescence were collected as stacks that can be visualized in a form that enables a three-dimensional perspective on the relationship of the knee structures; see Figs. 2 (Video 3) and 3 (Video 4).

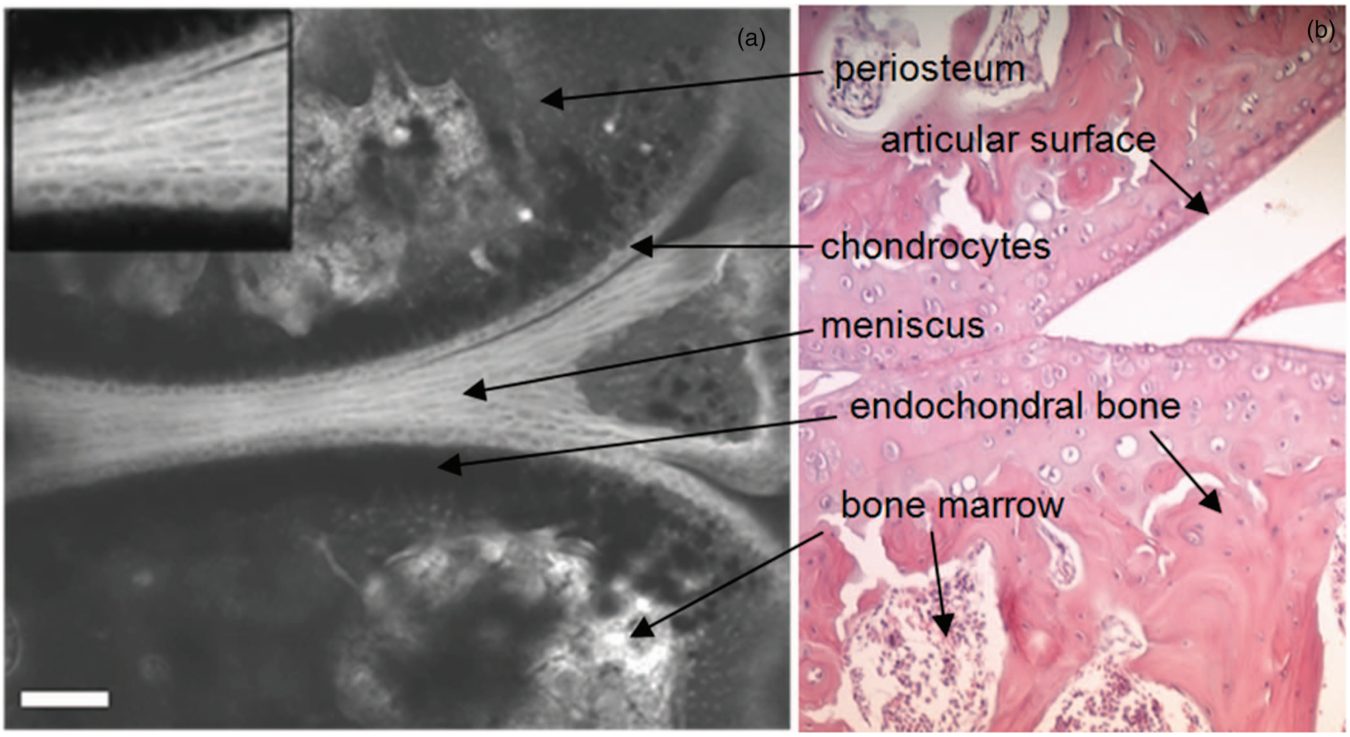

**Fig. 2** (a) Multiphoton microscopy image of intrinsic fluorescence in mouse knee at a depth of 1.03 mm from image stack (Video 3). Inset amplifies articular surface to illustrate detailed resolution. (b) H&E section of the same specimen at comparable magnification (20× objective). Scale bar is 100 $\mu$m. (Video 3, MPEG, 1.75 MB) [URL: http://dx.doi.org/10.1117/1.3641992.3]

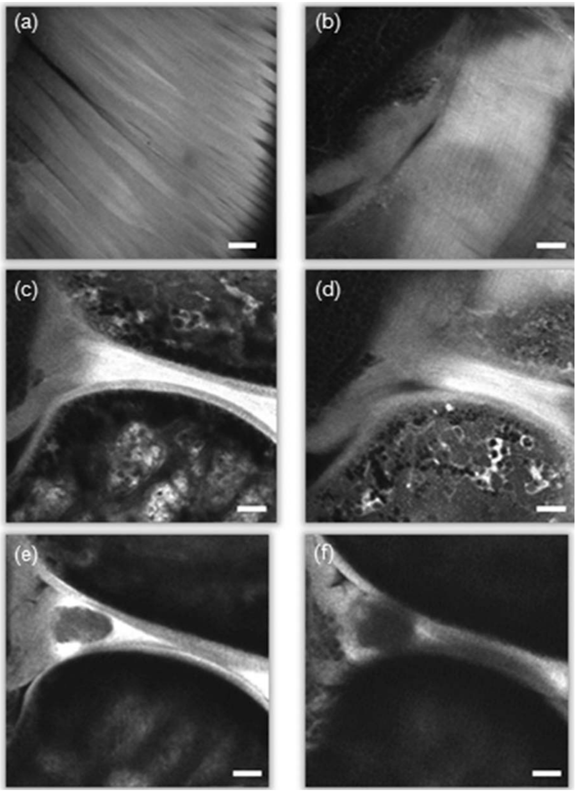

**Fig. 3** Frame excerpts of whole mouse knee 3D volume at depths of (a) 210 $\mu$m, (b) 290 $\mu$m, (c) 335 $\mu$m, (d) 420 $\mu$m, (e) 525 $\mu$m, and (f) 695 $\mu$m (Video 4). Scale bars = 100 $\mu$m (Video 4, MPEG, 3.49 MB). [URL: http://dx.doi.org/10.1117/1.3641992.4]

Muscle fibers [Fig. 3(a)] overlie tendinous fascia [Fig. 3(b)] which transition to bone covering cartilage and bone marrow [Figs. 3(c) and 3(d)]. The meniscus thins and the articular surfaces approach each other deeper into the joint [Figs. 3(d) and 3(e)]. Clear multiphoton intrinsic fluorescence images were obtainable on clarified tissue through fat, muscle, fascia, bone, and cartilage. Although the peak intensity of each image in the stack was normalized, at 1.3 mm of depth, some loss of signal is evident. A three-dimensional volumetric reconstruction can be easily manipulated to provide a broader view of the structural relationships; see Fig. 4 (Video 5) and (Video 6).

A large vessel can be noted lying atop the surface muscle with clear individual muscle fibers and $z$-line definition (muscle contraction zones) [Fig. 4(a)]. Developing bone marrow elements in three-dimensional aggregates are identifiable within the subchondral ossification center [Figs. 4(b) and 4(c)]. Of note, the only additional image manipulation required for 3D reconstruction was normalization of image intensity at different depths. The scanning process using the mechanical stage and galvanometer-mounted mirrors preserved location information accurately such that complicated image registration routines were not necessary. Removal of the muscle and fascia in the 3D reconstruction enables better visualization of the bone marrow islands in the subchondral space and of the meniscus sitting atop the cartilaginous capsule of the femur and tibia [Figs. 4(d) and 4(f)]. The synovial space and synovial tissue are also identifiable [Fig. 4(f)].

Additional structural information for the mouse knee joint was garnered by collecting SHG signals during MPM. The intrinsic fluorescence image extends from the articular cartilage (at bottom) to the growth plate (proliferation zone) and shaft of the long bone above it [Fig. 5(a)].

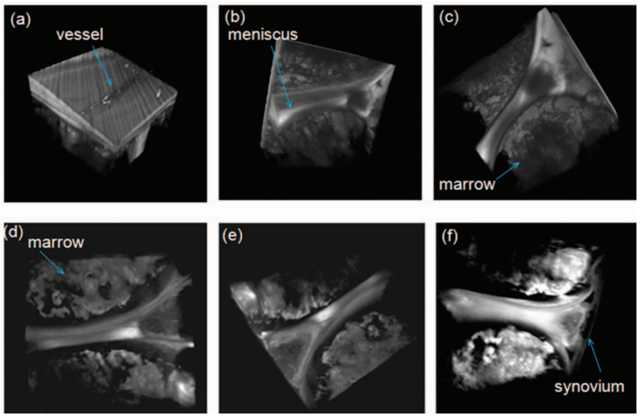

**Fig. 4** Still frames of three-dimensional volume reconstruction of whole knee. (a) Surface muscle fibers course diagonally. Perpendicular contraction zones are visible. (b) and (c) Underlying knee structures including cartilage, meniscus, and bone marrow (Video 5). (d)–(f) Removing muscle and fascia allows better visualization of cartilage and bone marrow as well as intrajoint tissue (Video 6) (Video 5, MPEG, 4.53 MB) [URL: http://dx.doi.org/10.1117/1.3641992.5]); (Video 6, MPEG, 4.53MB). [URL: http://dx.doi.org/10.1117/1.3641992.6]

The fluorescence image has been merged with the SHG microscopy signal colored in red. The SHG highlights cell-like structures located in the epiphysis, primarily subchondrally, and above the epiphyseal plate which likely represent sites of contrast-enhancing chondrocyte secretion as part of the ossification process [Fig. 5(b)]. This is a structural component that is not easily identified on MPM images or H&E slides, although similar structures in these areas can be noted in the H&E stained section [Fig. 5(c)].

FLIM was employed as a third modality during MPM and also produced clear images in clarified tissue at 1-mm depths. The lifetime allowed improved definition between the cellular cartilage component at the articular surface and the adjacent fibrous-cartilagenous meniscus [Fig. 6(a)].

Metabolically highly active bone marrow cells are identified as having a different lifetime than the surface chondrocytes

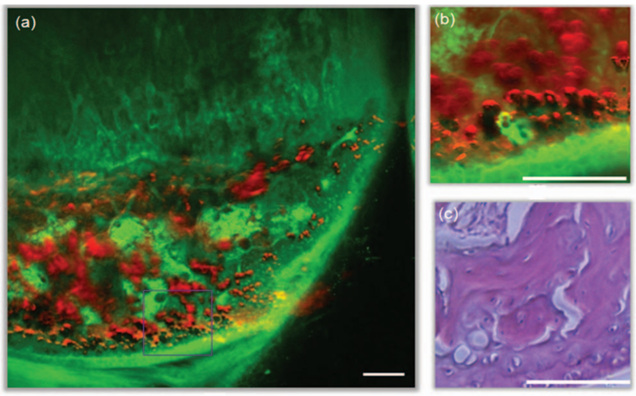

**Fig. 5** (a) MPM (green) and SHG (red) combined knee image. (b) Magnified squared boxed area of (a). (c) H&E image of same sample. Scale bars are (a) 100 $\mu$m and (b) and (c) 50 $\mu$m.

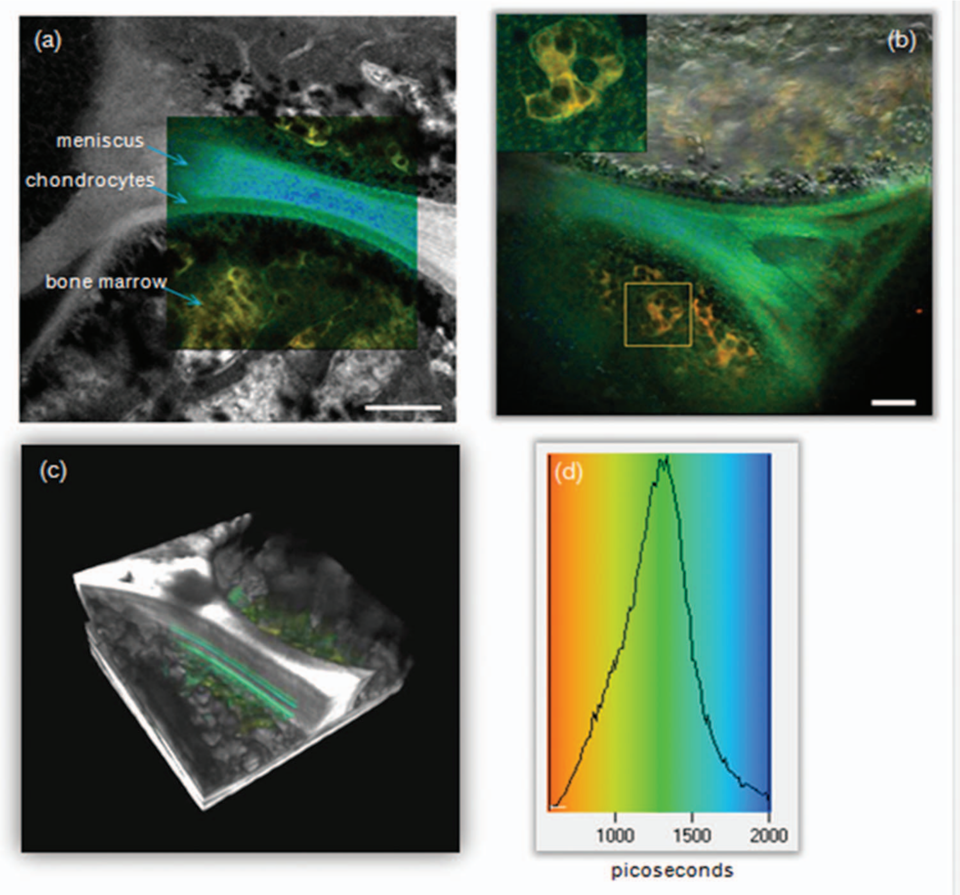

**Fig. 6** (a) Fluorescence lifetime image embedded in MPM image of mouse knee at 420 $\mu$m depth. (b) FLIM and SHG (gray) combined knee image. (c) 3D MPM/FLIM volume with corresponding lifetime histogram (d) (Video 7). Scale bars are 100 $\mu$m (Video 7, MPEG, 4.53 MB). [URL: http://dx.doi.org/10.1117/1.3641992.7]

[yellow, Fig. 6(a)]. Inspection of sections just deep to bone reveals intrinsically fluorescent structures with short fluorescent lifetimes that are not visible by MPM, H&E, or SHG [Fig. 6(b) and inset]. Merging with SHG demonstrates the relationship of these structures to the spherical components identified by SHG and to the periosteum, which suggests these represent a more advanced stage of ossification, perhaps newly secreted periosteum. The FLIM images were also intercalated into three-dimensional MPM stacks producing a volume rendering with enhanced images, illustrating the potential for 3D MPM/FLIM imaging; see Fig. 6(c) (Video 7).

## 4 Discussion

Multimodal MPM of cleared organs, including both SHG and FLIM, shows great promise as a tool of both basic research and clinical application. From the point-of-view of analyzing tissue specimen histology, MPM-clearing 3D reconstruction with SHG and FLIM provides an enhanced perspective on tissue growth, structure, and cellular composition which could prove useful in determining malignant or benign behavior and in assessing extent of disease spread within the context of microscopic anatomy, an often challenging aspect of histologic evaluation in biopsies. It also provides a method for comprehensive visual inspection prior to cutting. This can help guide slice selection and orientation for preparation of traditional histologic sections using the array of specialty stains developed for pathological evaluation, and can reduce considerably the risk that a relevant portion of the specimen is missed. Although some tissue shrinkage was observed as a result of the dehydration process, this did not appear to change the overall morphology. The methods used here were chosen based on previous successful results,[4] however, future work will explore alternative methods that may reduce shrinkage.

FLIM images of a clarified mouse testicle clearly delineated elastin in the extracellular matrix fromthe NADH in the spermatocytes and spermatozoa within seminiferous tubules at depths of ~1 mm. In this case, the lifetime of the elastin can be correlated with that of other cleared organs, such as lung (data not shown), which, combined with the morphological structure of the organ, unambiguously identifies the molecular source of the fluorescence signal. Differentiating the elastin and NADH fluorescence based simply on their emission spectra would be complicated by their large degree of overlap.

The combination of MPM fluorescence, SHG, and FLIM provided exquisite detail in imaging of the mouse knee at depths exceeding 1 mm. Imaging intact specimens enables construction of large 3D data sets without the need for complicated image registration algorithms. Importantly, it circumvents artifacts due to tissue damage during the sectioning process, a recurring problem in histology. Although the molecular sources of fluorescence for the FLIM images of the knee are not known, and can be difficult to identify with certainty, the contrast was nonetheless sufficient to identify several morphologically important and distinct structures. FLIM images of the knee clearly differentiated the meniscus from the adjacent chondrocytes and also isolated the signal from bone marrow. FLIM also identified periosteal structures that were not visualized by any other imaging modality, illustrating the potential of the technique to extract additional structural information with minimal added effort.

## 5 Summary and Conclusion

Multimodal imaging was achieved in clarified tissue producing rich informational content more than 1-mm deep into *ex vivo* tissue. This depth far exceeds that at which conventional confocal or multiphoton imaging can produce comparable images. The images were produced using only intrinsic signals, without the use of any organic or fluorescent dyes which might add cost or effort, introduce variability in signal, or interfere with subsequent analysis. Images with subcellular resolution were amenable to three-dimensional reconstruction without complex image registration procedures. The SHG and FLIM imaging complemented multiphoton fluorescence images, providing additional structural and cellular information also without the need for staining, further tissue manipulation, or other type of special preparation. Analyzed specimens were then processed as routine pathology specimens without any recognizable artifacts, making them available for traditional stains such as H&E. This analysis demonstrates the feasibility of combining MPM, SHG, and FLIM in clarified tissue for three-dimensional reconstruction of tissue more than 1-mm thick as an adjunct to traditional histologic analysis, thus maximizing informational content in research and clinical pathology samples.

## *References*

1. J. A. N. Buytaert and J. J. J. Dirckx, "Design and quantitative resolution measurements of an optical virtual sectioning three-dimensional imaging technique for biomedical specimens, featuring two-micrometer slicing resolution,"*Biomed. Opt.* **12**(1), 014039 (2007).
2. C. Pitris, K. T. Saunders, J. G. Fujimoto, and M. E. Brezinski, "High-resolution imaging of the middle ear with optical coherence tomography: A feasibility study," *Arch. Otolaryngol. Head Neck Surg.* **127**(6), 637–642 (2001).
3. M. Capek, P. Bruza, J. Janacek, P. Karen, L. Kubinova, and R. Vagnerova, "Volume reconstruction of large tissue specimens from serial physical sections using confocal microscopy and correction of cutting deformations by elastic registration," *Microsc. Res. Tech.* **72**(2), 110–119 (2009).
4. S. G. Parra, T. H. Chia, J. P. Zinter, and M. J. Levene, "Multiphoton microscopy of cleared mouse organs," *J. Biomed. Opt.* **15**(3), 036017 (2010).
5. T. Abraham, S. Wadsworth, J. M. Carthy, D. V. Pechkovsky, and B. McManus, "Minimally invasive imaging method based on second harmonic generation and multiphoton excitation fluorescence in translational respiratory research," *Respirology* **16**(1), 22–33 (2011).
6. M. L. C. Wu, V. S. Varga, V. Kamaras, L. Ficsor, A. Tagscherer, Z. Tulassay, and B. Molnar, "Three-dimensional virtual microscopy of colorectal biopsies," *Arch. Pathol. Lab Med.* **129**(4), 507–510 (2005).
7. T. A. Freeman, P. Patel, J. Parvizi, V. Antoci, and I. M. Shapiro, "Micro-CT analysis with multiple thresholds allows detection of bone formation and resorption during ultrasound-treated fracture healing," *J. Orthop. Res.* **27**(5), 673–679 (2009).
8. O. R. Karabacak, E. Cakmakci, U. Ozturk, F. Demirel, A. Dilli, B. Hekimoglu, and U. Altug, "Virtual cystoscopy: the evaluation of bladder lesions with computed tomographic virtual cystoscopy," *Canadian Urological Assoc. J.* **5**(1), 34–37 (2011).
9. Y. A. Bhagat, C. S. Rajapakse, J. F. Magland, J. H. Love, A. C. Wright, M. J. Wald, H. K. Song, and F. W. Wehrli, "Performance of mu MRI-based virtual bone biopsy for structural and mechanical analysis at the distal tibia at 7T field strength," *J. Magn. Reson Imaging* **33**(2), 372–381 (2011).
10. T. Ragan, J. D. Sylvan, K. H. Kim, H. Huang, K. Bahlmann, R. T. Lee, and P. T. C. So, "High-resolution whole organ imaging using two-photon tissue cytometry," *J. Biomed. Opt.* **12**(1), 014015 (2007).
11. P. S. Tsai, B. Friedman, A. I. Ifarraguerri, B. D. Thompson, V. Lev-Ram, C. B. Schaffer, Q. Xiong, R. Y. Tsien, J. A. Squier, and D. Kleinfeld, "All optical histology: Serial ablation and multiphoton imaging of neuronal tissue with femtosecond laser pulses," *IEEE Leos Annual Meeting Conference Proceedings*, Vols. 1 and 2, pp. 485–486 (2003).
12. F. Helmchen and W. Denk, "Deep tissue two-photon microscopy," *Nat. Methods* **2**(12), 932–940 (2005).
13. W. R. Zipfel, R. M. Williams, and W. W. Webb, "Nonlinear magic: multiphoton microscopy in the biosciences," *Nat. Biotechnol.* **21**(11), 1368–1376 (2003).
14. W. Denk, J. H. Strickler, and W. W. Webb, "2-Photon laser scanning fluorescence microscopy," *Science* **248**(4951), 73–76 (1990).
15. P. Theer, M. T. Hasan, and W. Denk, "Two-photon imaging to a depth of 1000 mu m in living brains by use of a Ti : Al2O3 regenerative amplifier," *Opt. Lett.* **28**(12), 1022–1024 (2003).
16. D. Kobat, M. E. Durst, N. Nishimura, A. W. Wong, C. B. Schaffer, and C. Xu, "Deep tissue multiphoton microscopy using longer wavelength excitation," *Opt. Express* **17**(16), 13354–13364 (2009).
17. W. Spalteholz, *Uber das Durchsichtigmachen von menschlichen und tierischen Praparaten* (About the transparency of human and animal preparations), S. Hierzal, Leipzig (1914).
18. H. U. Dodt, U. Leischner, A. Schierloh, N. Jahrling, C. P. Mauch, K. Deininger, J. M. Deussing, M. Eder, W. Zieglgansberger, and K. Becker, "Ultramicroscopy: three-dimensional visualization of neuronal networks in the whole mouse brain," *Nat. Methods* **4**(4), 331–336 (2007).
19. J. Huisken, J. Swoger, F. Del Bene, J. Wittbrodt, and E. H. K. Stelzer, "Optical sectioning deep inside live embryos by selective plane illumination microscopy," *Science* **305**(5686), 1007–1009 (2004).
20. V. V. Tuchin, "A clear vision for laser diagnostics (review)," *IEEE J. Sel. Top. Quantum Electron.* **13**(6), 1621–1628 (2007).
21. R. C. Ecker, R. de Martin, G. E. Steiner, and J. A. Schmid, "Application of spectral imaging microscopy in cytomics and fluorescence resonance energy transfer (FRET) analysis," *Cytometry, Part A* **59A**(2), 172–181 (2004).
22. T. Zimmermann, "Spectral imaging and linear unmixing in light microscopy," in *Microscopy Techniques*, pp. 245–265, Springer-Verlag, Berlin (2005).
23. A. J. Radosevich, M. B. Bouchard, S. A. Burgess, B. R. Chen, and E. M. C. Hillman, "Hyperspectral in vivo two-photon microscopy of intrinsic contrast," *Opt. Lett.* **33**(18), 2164–2166 (2008).
24. J. R. Lakowicz, *Principles of Fluorescence Spectroscopy*, 3rd. Ed., Plenum Press, New York (1999).
25. H. D. Vishwasrao, A. A. Heikal, K. A. Kasischke, and W. W. Webb, "Conformational dependence of intracellular NADH on metabolic state revealed by associated fluorescence anisotropy," *J. Biol. Chem.* **280**(26), 25119–25126 (2005).
26. J. R. Lakowicz, H. Szmacinski, K. Nowaczyk, and M. L. Johnson, "Fluorescence lifetime imaging of free and protein-bound NADH," *Proc. Natl. Acad. Sci. U.S.A.* **89**(4), 1271–1275 (1992).
27. T. H. Chia, A. Williamson, D. D. Spencer, and M. J. Levene, "Multiphoton fluorescence lifetime imaging of intrinsic fluorescence in human and rat brain tissue reveals spatially distinct NADH binding," *Opt. Express* **16**(6), 4237–4249 (2008).
28. W. R. Zipfel, R. M. Williams, R. Christie, A. Y. Nikitin, B. T. Hyman, and W. W. Webb, "Live tissue intrinsic emission microscopy using multiphoton-excited native fluorescence and second harmonic generation," *Proc. Natl. Acad. Sci. U.S.A.* **100**, 7075–7080 (2003).
29. A. Zoumi, X. A. Lu, G. S. Kassab, and B. J. Tromberg, "Imaging coronary artery microstructure using second-harmonic and two-photon fluorescence microscopy," *Biophys. J.* **87**(4), 2778–2786 (2004).
30. T. A. Pologruto, B. L. Sabatini, and K. Svoboda, "ScanImage: flexible software for operating laser scanning microscopes," *Biomed. Eng. Online* **2**, 13 (2003).